First life vs. Second life of lithium-ion batteries in consumer applications: evaluating performance degradation during extended usage through postmortem analysis

By

Shashank Arora*[a], Vidhula Ahire[b], Eeva Leena Rautama[c], Katja Lahtinen[c], Tanja Kallio[c], Kari Tammi[a], Panu Sainio[a]

* corresponding author: Shashank Arora (shashank.arora@aalto.fi)

[a] Department of Mechanical Engineering, Aalto University, Espoo, Finland – 02150

[b] Centre de Recherche sur les Ions, les Matériaux et la Photonique (CIMAP), Normandie Univ/ENSICAEN/UNICAEN/CEA/CNRS, Caen, France

[c] Department of Chemistry and Material Sciences, Aalto University, Espoo, Finland - 02150

First life vs. Second life of lithium-ion batteries in consumer applications: evaluating performance degradation during extended usage through postmortem analysis

Abstract

A new regulation proposed by European Commission requires that all batteries available in the European Union market are safe throughout their cycle life. However, consumer devices, including the high-end systems, do not display the state-of-health (SOH) of their battery. Further, the devices can be "non-certified" items and typically use lithium cobalt oxide (LCO) batteries, a chemistry that is less stable than other Li-ion battery chemistries. The battery research so far has not delved into the behaviour of cells aged more than 80% of their initial capacity. Consequentially, there is limited information available regarding what to expect if the user continues to use their battery powered device beyond this limit. Above combinations can put the user at financial as well as serious physical risks.

This paper focuses on life beyond SOH 80% and aims to provide some evidence that can be used to determine the stage till which the LCO batteries can be treated as "safe to use". We use galvanostatic cycling and postmortem analysis as tools in this investigation. It is revealed that a significant cell-to-cell variation and a large volume increase are the two major issues that can affect performance and safety ratings of the state-of-the-art commercial LCO batteries during extended cycling.

1. Introduction

The number of battery-powered consumer appliances in our surrounding has increased exponentially in recent years [1]. Importantly, their manufacturing designs have changed appreciably due to miniaturization requirement [2, 3]. This requires batteries with high power

and energy densities, reliable cycle life and lightweight packaging [4, 5]. Therefore, preferential battery chemistry for consumer applications remains lithium cobalt oxide (LCO; chemical representation - $LiCoO_2$). Schmidt *et al.'s* recent research validates the selection [6]. In a systematic study comparing various commercially available cells, they confirm that presently LCO/graphite system is the only viable option if the goal is to have high power density without compromising on energy density.

Battery behavior is sensitive to stimuli like charge/discharge currents, cut-off voltages, state-of-charge (SOC) and ambient temperature fluctuations. Duty cycle or usage pattern is another key variable that influences long-term performance of batteries [7, 8]. Moreover, battery cells can age differently whilst assembled as "battery packs" in comparison to when being used in isolation [9]. Consequentially, multiple standards have been created to guide design, development and usage of battery-powered electronic systems. Some of these standards are:

- IEEE 1625 - Standard for Rechargeable Batteries for Multi-Cell Computing
- IEEE 1725 - Standard for Rechargeable Batteries for Mobile Telephones
- ASTM F963 - Standard Consumer Safety Specification for Toy Safety
- ASTM F2951 - Standard Consumer Safety Specification for Baby Monitors
- UL 1642 - Standard for Safety for Lithium Batteries
- UL 2054 - Standard for Household and Commercial Batteries
- UL 2056 - Outline of Investigation for Safety of Power Banks
- UL 2595 – Standard for Safety for General Requirements for Battery-Powered Appliances
- UL 4200A - Standard for Safety for Products that Incorporate Button or Coin Cell Batteries Using Lithium Technologies
- UL 60065 - Standard for Audio, Video, and Similar Electronic Apparatus–Safety Requirements

- ANSI/NEMA C18 - Safety Standards for Primary, Secondary and Lithium Batteries
- ANSI/CAN/UL 2272 - Electrical Systems for Personal E-Mobility Devices

Per these, enhanced safety features must be integrated to mitigate potential risks involved in handling and using the volatile compounds contained in batteries. Nevertheless, numerous incidents of battery failure and catching fire due to system overheating and electrical short-circuit have been reported till date. Millions of lithium-ion (Li-ion) battery-powered products including electric scooters and hoverboards have been recalled owing to this. A list of major product recalls is available from [10]. Point to note is that standards are not mandatory rules but "optional" recommendations; hence, they cannot be enforced [11]. This means that a large portion of battery failure events can be attributed to the fact that consumer appliance market is largely unregulated. Consequentially, many "uncertified" battery-powered products may reach the market without undergoing proper testing for their intended application or whilst connected to the charging station.

An aged battery generates more heat than pristine ones [12-14]. Left unchecked, this can become a major safety risk for the end-user and for the first responders [15, 16]. Therefore, usual practice in electric vehicle (EV) industry is to replace a battery pack as soon as its state-of-health (SOH) becomes 80% of the original capacity [17]. This is called end-of-life (EOL) criterion. No such criterion or guideline, however, exists for consumer appliances. Establishing the EOL guideline for portable electronic devices is vital as LCO material exhibits the lowest thermal stability amongst all commercial cathode materials [18]. Thermal stability of a lithium metal oxide cathode refers to its tendency to release oxygen exothermically when heated beyond a certain temperature. The released oxygen reacts with organic materials in the battery electrolyte leading to onset of thermal runaway. For LCO cathodes, this typically happens above 200 °C [19, 20].

Zhang compared impedance spectra of fully charged 2.4 Ah commercial 18650-type LCO cells cycled 100 times, 200 times and 300 times to that of the pristine cells. Capacity fade in cycled cells was attributed to increase in charge transfer resistance [21]. Important to note here is that Zhang does not explicitly report SOH for any of the tested cells but derived values for the cells cycled 300 times suggest that their SOH was significantly lower than the EOL cut-off used in EV applications. Still, no comments were provided on physical state of these cells at the end of the test schedule. Therefore, it is not clear if visual signs of any kind of structural damage to cell packaging were noticed during or after testing.

Guan *et al*. performed accelerated cycle life tests using discharge rates ranging from 0.6C to 3C on 1.15 Ah commercial prismatic cells containing LCO cathode and mesocarbon microbead anode. Tests were terminated when the discharge capacity dropped to SOH 80. It is concluded that cycling does not lead to bulk transformation in LCO batteries, but significant microstructural modifications can be typical [22]. Barcellona and Piegari studied the effect of current on 10 Ah LCO thin pouch cells. The cells were cycled between SOC 20 and SOC 80 at 0.8C, 2.5C and 5C rates. Cell temperature was controlled between 20 – 30 °C via peltier coolers [23]. Note that the SOH of the most degraded cell in their investigation was higher than 94%. Their results show that capacity fade rate above SOH 95 is independent of C-rate if the cell is not over charged or deep discharged and its temperature is maintained in an appropriate window.

Zhang *et al*. studied degradation behavior of full cells made from blended cathodes (LCO + NMC532) and graphite anode. While cycling at 1C-rate, they observed a largely linear capacity fade in all the tested cells. The cycling was stopped after 700 continuous cycles. Corresponding SOH was 78.5% [24]. Schmidt *et al*. cycled high-power LCO pouch cells of different cell designs, sourced from different manufacturers, up to 70% SOH. Much of the tested set completed 1500 cycles (both charging and discharging at 1C) before reaching SOH 70. There

were only two outliers whose capacity faded to 70% within 200 and 850 cycles, respectively. In contrast, a large variability was observed in high power discharge conditions – some cells completed only 100 cycles whereas other cells performed up to 2600 cycles [6]. They, as well, did not report any structural or mechanical deformation in aged cells that may indicate a safety risk for the battery user.

Roth and Doughty investigated thermal response of 18650 commercial LCO cells with unknown history [25]. Their work highlights the serious issue of increased gas formation with battery aging. Continuous gas generation in batteries can cause premature mechanical failure. They noted that batteries experiencing this issue can vent hot, flammable, and toxic gaseous emissions to the environment even at low SOCs, which is a major safety challenge. Larsson *et al.* cycled eight 6.8 Ah commercial LCO cells at 0.5C rate in ambient temperature environment. Three cells were cycled 100 times, two were cycled 200 times, another two were cycled 300 times while the last remaining cell failed suddenly after the 229th cycle. SOH of the cells cycled 300 times were 89.1% and 89.4%, respectively [26]. Thickness of these cells remained unchanged during the cycling procedure.

Battery aging has been a topic of great interest and several researchers have investigated degradation mechanisms for different Li-ion battery chemistries [27-40]. However, cycling tests were stopped at SOH 80 in majority of these investigations. Consequently, no documented evidence of safety beyond the SOH 80 of battery cells, particularly those that are designed using a thermally less stable chemistry such as LCO, is available from the published literature. Purpose of this paper is to serve as that evidence. This is important considering a new regulation proposed by the European Commission aims to ensure that all the batteries placed in the EU market are safe throughout their cycle life [41]. Moreover, portable electronic devices, including the premium ones, rarely display SOH of their battery owing to which their users can sometimes get caught off guard. Therefore, this paper presents results from experiments that

were conducted with an intent to understand the LCO battery degradation rate and mechanism during their second life and to answer the question – "are these batteries safe to use beyond the usual 80% remaining useful life as an EOL criterion?".

2. Experimental Methods

Thirty commercially available pouch-shaped Li-ion cells of 0.93 Ah nominal capacity were sourced from AEC, China. They have LCO cathode and graphite anode. Key parameters from the cell's technical specification sheet are listed in Table 1.

Parameter	Value
Nominal Voltage	3.7V
Minimum Capacity	0.9 Ah
Maximum continuous charge current	0.465 A
Maximum continuous discharge current	0.93 A
Expected cycle life	>80% of initial capacity after 500 cycles
Initial thickness	5.15 mm
Maximum thickness after 500 cycles	5.74 mm

Table 1 – Key specifications of 0.93 Ah AEC pouch cell

2.1. Cycle life tests

The test matrix was divided into seven groups (A - G). Groups A to F contained four cells each to ensure that the obtained results were statistically reliable. The last group (G), however, contained six cells to increase the sample set size further in the domain of primary interest (SOH < 80%, referred hereafter as "second life" region). To begin, all cells in the matrix underwent a galvanostatic characterization cycle (both charging and discharging processes) at 0.1C to determine their initial or beginning of life (BOL) capacities. Thereafter, they were cycled between the cut-off voltages of 2.7 V and 4.2 V a specific number of times in room temperature environment on a programmable Neware battery testing station. The number of aging cycles for each group is available in Table 2. Constant current-constant voltage program (CC-CV) was used for charging. Current tapered to C/20 value in the CV-phase. Each cycle began from SOC 0. Average room temperature was 23.5 °C with a seasonal temperature variation of ± 4°C.

C-rates of 0.5C and 1C, which are the maximum permissible rates per the cell's technical specification sheet for charging and discharging, respectively, were used. Klett *et al.* demonstrated that constant current cycling in full SOC range (0-100%) induces the most severe degradation in cell performance [42]. Therefore, this procedure was adopted in our work to re-create the worst-case aging scenario for the battery cells. One-minute rest was included between charge and discharge steps. SOH decay was measured at regular intervals of 100 cycles through a slow (0.1C) galvanostatic charge/discharge test. In the end, all the battery cells exiting the test matrix were discharged at 0.01C to prepare for subsequent post-mortem analysis.

Galvanostatic characterization tests (at BOL as well as at intermediate stages) were followed up with electrochemical impedance spectroscopy (EIS) checkups at SOC 50 level to obtain supporting parameter values. Note that instead of the nominal capacity, discharge capacity measured from the previous cycle was used for SOC calculation for these checkups. Prior to conducting the EIS tests, the battery cells were held in an open-circuit state for 10 hours in room temperature. The EIS spectra were recorded in potentiostatic mode with 5 mV voltage perturbation and the frequency range used was 10 kHz to 10 mHz. A Metrohm Autolab potentiostat (PGSTAT100) and an Autolab frequency response analyzer were used for this purpose.

2.2. Post-mortem analysis

A combination of methods like X-ray diffraction (XRD), scanning electron microscopy (SEM), energy dispersive x-ray (EDX) along with focused ion beam (FIB) was applied to evaluate typical battery aging indicators like particle cracking, thickening of solid electrolyte interphase (SEI) film, phase transformation, etc.

To prepare samples, fully discharged LIBs were transferred to an argon filled glove box (< 10 ppm O_2) for disassembly. The packaging was carefully cut using a pair of ceramic scissors to reveal a prismatic-type electrode winding. The electrode winding was then pulled out of the

packaging and unwound slowly using plastic tweezers. Unwound electrodes were washed three times with anhydrous dimethyl carbonate (DMC, Sigma-Aldrich) of ≥99% purity to remove the electrolyte salt residues. After washing, they were left to dry in the argon atmosphere of the glove box for several minutes. Appropriately sized samples were then cut out from the internal sections (close to the tab) of the electrode winding for post-mortem analysis. The harvested samples were taken out from the glovebox in dry, gas-tight containers and various tests were scheduled to minimize exposure to moisture and ambient air.

To investigate changes in the precise elemental composition, the samples were investigated with atomic absorption spectroscopy (AAS, Varian AA240) and inductively coupled plasma optical emission spectroscopy (ICP-OES, Perkin Elmer 7100DV). To prepare the samples for the measurements, they were first weighted (about 200 mg) in teflon vessels. Then, hydrochloric acid (HCl, 7.5 ml, conc) and nitric acid (HNO_3, 2.5 ml, conc) were added and the vessels were closed and placed in microwave oven (Milestone Ethos). Samples were heated to 200 °C for 1 h. After cooling, they were diluted with Milli-Q water and Li was determined with AAS using flame atomization while cobalt concentration was determined with ICP-OES. The crystal structures and bulk phase transitions, on the other hand, were characterized by means of XRD with a PANalytical X'Pert Pro MPD Alpha-1 diffractometer using Cu $K_{\alpha 1}$-radiation with a wavelength of 0.15406 nm. The intensities and scattering angles of the diffracted X-rays were recorded in a 2θ range of 10–90°. The step size employed was 0.0131°. The changes in the particle sizes and morphologies were assessed using SEM and EDX (Tescan Mira-3). Acceleration voltages of 5 kV and 20 kV were used for the SEM and the EDX analyses, respectively. Prior to SEM measurement, the samples were sputter coated with Pd/Au (20/80) to improve electrical conductivity and, in turn, to better facilitate image analysis. Supporting information was derived from cross-sectional images obtained after milling the electrode samples with a focused Ga-ion beam in a Joel JIB-4700F multi-beam system. A 1 μm thick Pt

layer was deposited on top of the electrode coating to protect the upper edges of the active material particles during milling as well as to reduce the curtaining artefacts. Intersection angle for the electron beam and the ion beam columns was fixed at 53°. First, a coarse ion beam of 10 nA was used to create a viewing channel for cross-section SEM. Then, the exposed cross-section area was fine polished sequentially with low intensity probe currents of 1 nA and 0.5 nA, respectively. The FIB-SEM images were captured using 5 kV accelerating potential.

Lastly, Ø 14 mm working electrodes for LCO and graphite half-cells were punched from the inner-most flap of the respective electrode winding, i.e., the electrochemically active section closest to the electrode tab. They were assembled in a standard CR2016-type casing (Hohsen Corp.) by pairing the harvested sample with a disc-shaped lithium metal counter electrode (Alfa Aesar) of 0.75 mm thickness and Ø 17 mm. Separator was 0.26 mm thick, Ø 19 mm glass fibre sheet (Whatman GF/A). 200 µl of commercial 1 M lithium hexaflurophosphate ($LiPF_6$) dissolved in 1:1 wt.% mixture of ethylene carbonate (EC) and dimethyl carbonate (DMC) (LP30, BASF) was added as an electrolyte. A stainless-steel spacer (0.2 mm thick, MTI) helped complete this assembly. Half-cells from at least three different commercial cells from the selected groups were assembled. Further, two or more half cells, wherever possible, were prepared from respective electrodes of each of these commercial cells. The whole process was performed in dry, argon atmosphere with both O_2 and H_2O levels below 1ppm. The assembled coin cells were then withdrawn from the glovebox and allowed to stabilize in room temperature for 24 h before proceeding to electrochemical testing on Neware battery cycler. Graphite half-cells were cycled three times with a charging and discharging current of 0.12 mAh between a voltage range of 0.01 and 1 V vs. Li^+/Li. In contrast for the LCO half-cell, the cycling current was 0.15 mAh and the voltage range was 2.7 to 4.3 V vs. Li^+/Li.

3. Results and Discussion
3.1. Preliminary characterisation and First life

Owing to limited number of testing channels, all LCO cells could not be cycled simultaneously. Resultantly, some cells experienced calendar aging (CA). BOL impedance plots recorded for various cells entering the test matrix are presented in Fig. 1a. Cells with prefix "F" in their nomenclature (legend) represent those that were connected to the tester soon after procurement whereas those identified with a prefix "CA" had to wait up to ten months for their turn for cycling. The size of the semicircles observed in the Nyquist plots is quite similar for all samples. No visible impedance rise during the storage period indicates that the LCO material did not suffer any obvious structural transformation during this time. This also means that the effect of calendar aging on battery degradation can be neglected (with acceptable risks) in this study. Correspondingly, cells in the aging test matrix were expected to have comparable performances and cycle lives. This is verified through capacity degradation plots on Fig. 1b.

Discharge capacity retention curves representative of the behaviour exhibited by the commercial LCO cells during their first life, defined as SOH > 80%, are presented in Fig. 1b. Noteworthy is that the energy storage capacity delivered by each cell at the BOL was larger than the nominal capacity (0.93 Ah) published in technical specification datasheet. However, a more critical observation relates to cell-to-cell variations. A difference greater than 3.5 % is observed amongst the BOL discharge capacities of different cells. In real life applications, cell-to-cell inconsistencies are responsible for a significant number of pack failures. Consequently, battery cells are sorted into groups containing cells with similar characteristics and performance ratings before pack assembly. Complex and sophisticated battery management systems are needed to manage operation of battery packs containing cells with substantially different available capacities [43]. This is a costly investment. Variation larger than 5% between the capacities of the strongest cell and the weakest cell of the pack is therefore not acceptable in practice.
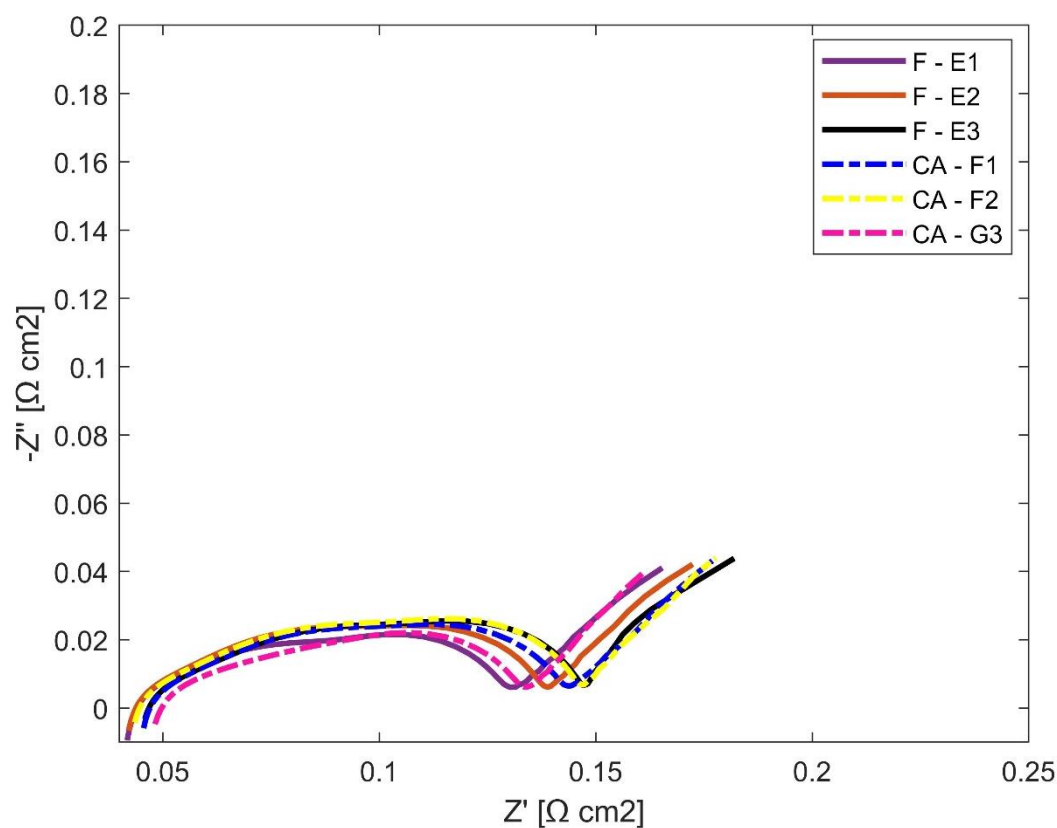
(a)
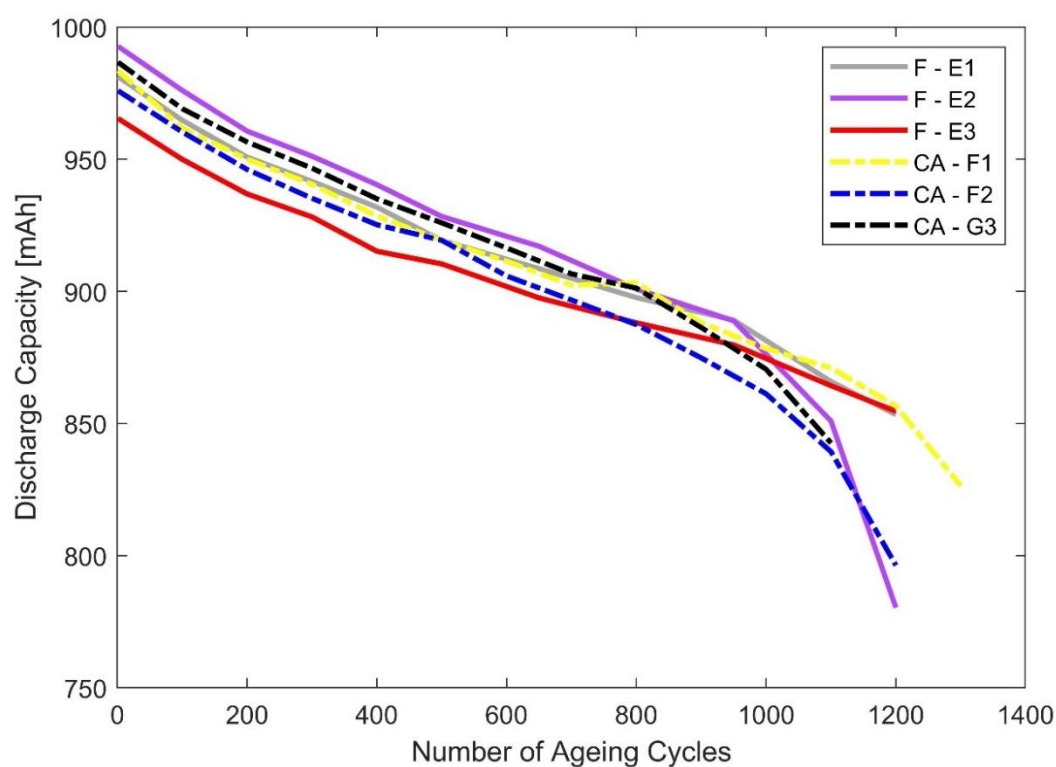
(b)

Figure 1 – (a) Comparison of BOL impedance measured at SOC 50 for the fresh LCO cells (denoted by prefix "F" in the legend) versus those that were calendar aged before being subjected to cycle life testing (denoted by prefix "CA"), and (b) capacity decay trend recorded for these cells during their first life.

Other important point to note is that the manufacturer-specified cycle life for these cells is 500 cycles. Discharge capacity of Sony 18650S cells at room temperature is known to degrade by 30% during 800 cycles [44]. However, as seen from the figure, the first life LCO cells tested in this study delivered at least 1200 cycles before dropping to SOH 80, i.e., more than twice the promised performance in terms of cycle life. Visibly, even the worst performing, calendar aged cell in this study (cell # G5) completed 900 aging cycles before experiencing a rapid drop in capacity near the SOH 80 mark. This is remarkable considering that the discharge rate used here was aggressive compared to the standard test conditions used by the manufacturer (1.0C vs. 0.5C). The longer cycle life measured in this study could be a direct result of careful material selection by the cell manufacturer. Modifications in chemistry, such as use of doping, or in physical properties, such as particle size and morphology, can lead to enhanced performance compared to the original specs given. Using coated cathode particles instead of bare particles in cell manufacturing has definite advantages as well [45]. For example, application of a Li permeable Al_2O_3 surface coating, as thin as 2 nm, can suppress cobalt dissolution and extend the cyclability of LCO batteries by more than 250% [46]. Similarly, $LiAlO_2$ coating can increase stability and ionic conductivity of LCO particles at high voltages and has proved even more effective than Al_2O_3 coatings in improving performance as well as rate capability of these batteries [47]. We detected trace amounts of aluminium in pristine graphite electrodes during postmortem analysis of our batch of LCO cells. This indicates that coating/doping could indeed be a possibility. More discussion follows in subsequent sections.

3.2. Second life – performance degradation

Fig. 2 depicts the performance decay trend during the entire life of the cycled LCO cells. It resembles a staircase curve. Appearance of a "knee" in the degradation curves marks the end of the first life whilst formation of an "elbow" somewhere in the second or the extended life region can be regarded as an indication to switch to a more moderate use case. Technically,

this means that the available discharge capacity drops linearly with the number of aging cycles for all the cells in the first life region and no abrupt behavior is observed. In contrast, the degradation behaviour in the second life region can be represented with a convex parabola, i.e., a quadratic function.

Table 2 shows the initial discharge capacity, EOL discharge capacity, number of cycles the cell was subjected to reach the exiting stage and the SOH at the end-of-test-routine for each of the thirty cells. The alphabets represent the number of cycles; A represents 0 cycles, B 25 cycles, C 200 cycles, D 700 cycles, E 1200 cycles. These are all first-life cells. Alphabets F and G, on the other hand, represent the second-life category. Due to varying aging rates, cells in the F-group and in the G- group have been cycled 1200 – 1700 times and 950 – 2200 times, respectively.

(a)
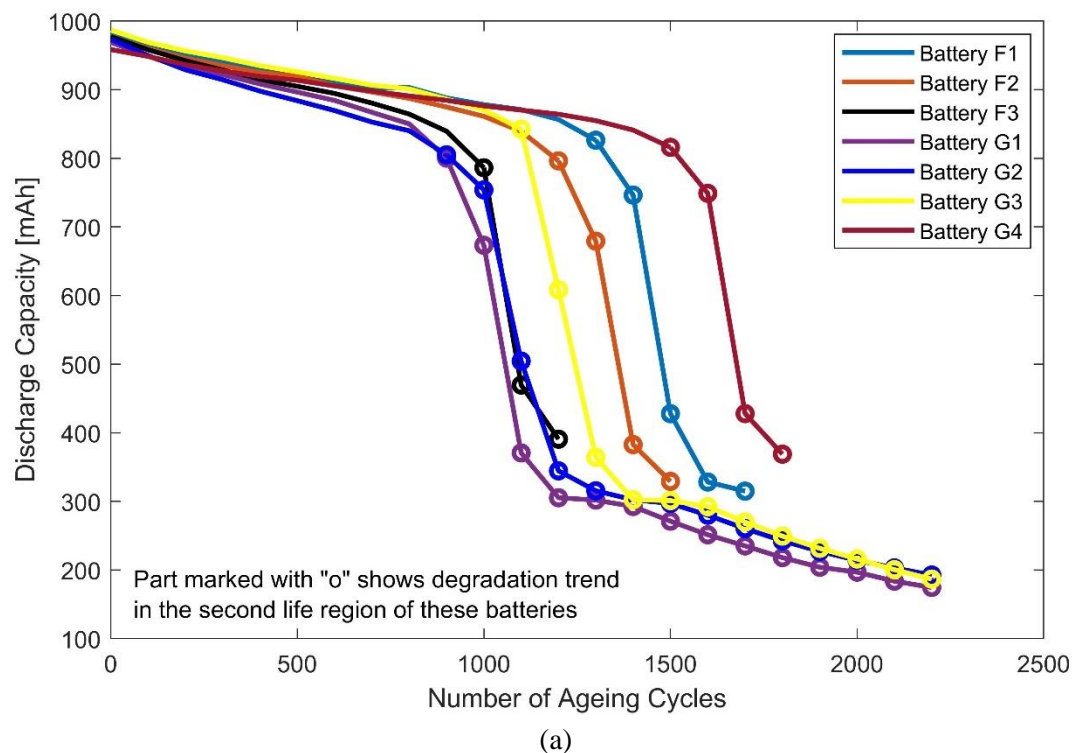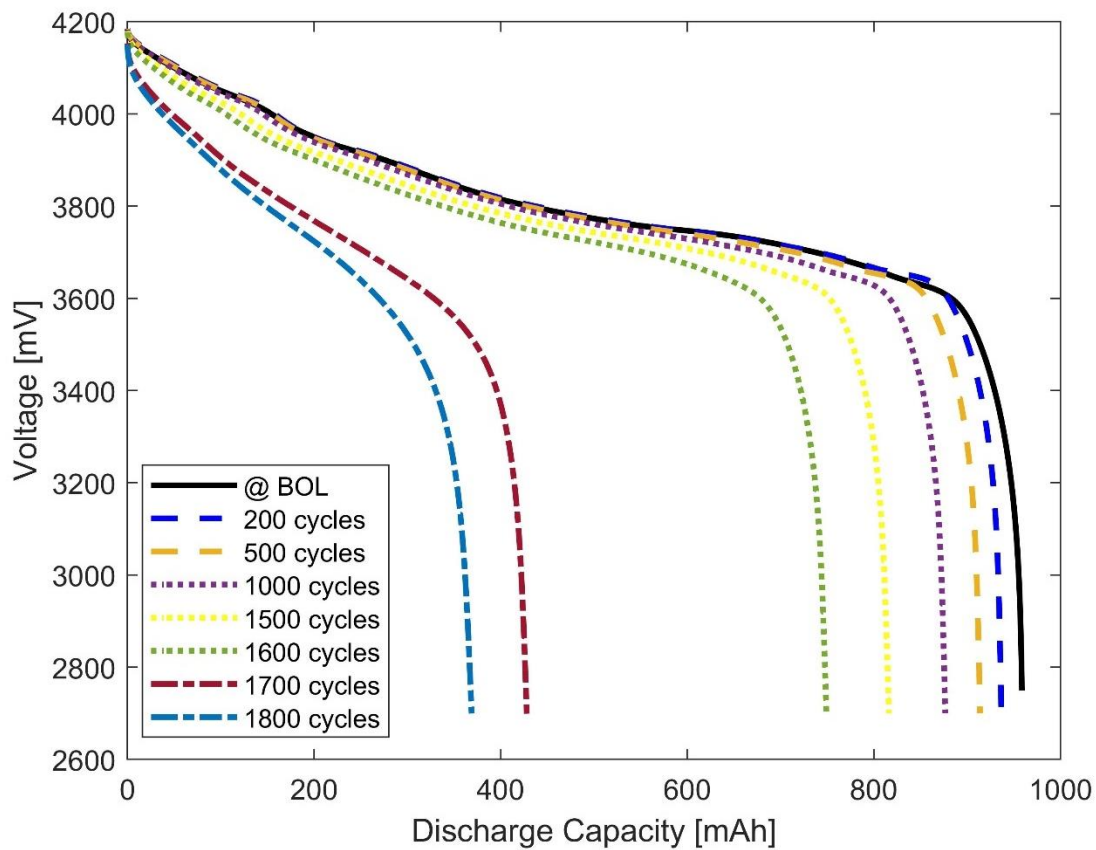
(b)

Figure 2 – (a) Discharge capacity degradation as a function of aging cycles for the second life cells – section marked with "o" represents the extended life region, and (b) corresponding voltage decay for one of the representative cells

Category	Group/Cell Number	Initial Capacity (mAh)	Number of aging cycles	Discharge Capacity at the exit stage (mAh)	State-of Health at the exiting stage
Pristine cells	A1	979.1	0	979.1	100%
	A2	976.4	0	976.4	100%
	A3	988.0	0	988.0	100%
	A4	977.7	0	977.7	100%
First life cells	B1	970.4	25	972.0	100.165%
	B2	969.3	25	971.6	100.237%
	B3	974.7	25	977.2	100.256%
	B4	958.7	25	971.1	101.293%
	C1	993.6	200	960.0	96.618%
	C2	986.9	200	959.7	97.244%
	C3	988.9	200	962.4	97.320%
	C4	975.9	200	948.9	97,233%
	D1	976.3	700	905.2	92.717%
	D2	973.5	700	912.6	93.744%
	D3	982.3	700	904.7	92.100%
	D4	979.1	700	905.9	92.523%
	E1	981.2	1200	853.3	86.965%
	E2	992.7	1200	780.3	78.604%

	E3	965.4	1200	854.6	88.523%
	E4	982.3	1200	874.2	88.995%
Second life cells	F1	983.5	1700	314.9	32.018%
	F2	975.9	1500	329.1	33.723%
	F3	977.3	1200	390.6	39.967%
	F4	971.6	1400	315.1	32.431%
	G1	969.1	2200	174.5	18.006%
	G2	973.4	2200	192.6	19.786%
	G3	986.7	2200	186.7	18.922%
	G4	958.5	1800	368.8	38.477%
	G5	973.3	950	507.8	52.173%
	G6	983.9	1050	510	53.10%

Table 2 – Summarized cycle life test results showing initial as well as EOL discharge capacity for each of the tested LCO cell along with the number of galvanostatic cycles (0.5C charge and 1C discharge) it was subjected to during the test regime.

The rate of capacity decay varies from cell-to-cell throughout the cycling. Consequently, the magnitude of variation in discharge capacities of the cells in the same group is different at different stages of life. It grows larger as the cells are aged. E.g., difference between the SOHs of the best performing cell and the worst performing cell in group C- is 0.7%. For D- group (cycled 500 times more than the cells in the C- group), the maximum difference is 1.6%, which is still acceptable. However, this difference exceeds 10% for the group E. Noteworthy is that three out of the four cells in this group had SOH > 86.95% at the end of 1200 cycles. One cell had a clearly more deteriorating performance, which lead to the stopped cycling for all cells in the group. This is akin to the control strategy used in EV applications where the weakest cell dictates performance output of the battery pack. For safety reasons, battery management system is often programmed to shut down pack operation as the regulatory parameters of any individual cell in the string drop below a pre-specified cut-off criterion [48].

It is obvious from these results that good cells with a decent amount of cycle life still left in them can get passed downstream as second life cells along with the faulty cell, i.e., the one that is truly below SOH 80 and at the end of its first life. "Sorting" is a popular strategy applied at this stage by pack integrators, to separate the good cells from the bad ones. It helps to reduce

inter-cellular variations in a battery module by categorizing cells with similar characteristics and assembling them together for the target application [49-56]. The results gathered in this study, however, suggest that cell sorting may be required more than once during the whole second life period. We see here that battery cells in their second life exhibit a behaviour that can be classified as "non-consistent" – in terms of cycles to achieve target SOH. Their degradation rates are steeper than those measured in the first life phase. For instance, the discharge capacity decays by almost the same percentage between the cycle numbers # 1501 and # 1600 for cell G4 as it did in the preceding 500 cycles (cycles 1001 - 1500). Thereafter, the absolute degradation value more than doubles in the next 100 cycles in the extended life phase (cycles 1601 - 1700). More importantly, the second life degradation rates differ substantially from one cell to another, as seen in Table 2. So much inherent variability can prove catastrophic for the second life battery packs. Therefore, it is recommended that sorting must be used at regular intervals or as frequently as feasible to maximize the pack performance and to minimize safety risks to the end user during the extended life region.

3.2.1. Observed impedance rise

Change in impedance during cycling aging of the LCO full cells was recorded with EIS. A comparative analysis of the impedance measured at the BOL and at the end of their first life (solid line type) versus change during the second life (dash line type) is presented in Fig. 3. Visual inspection of these plots revealed a heavily depressed semicircle (or an arc) indicating presence of one dominating aging mechanism at full cell level. Depression of the semicircle is correlated to porosity of the electrode microstructure. Previous EIS analyses of layered oxide electrodes have linked this semicircle to charge transfer on the cathode side. Above SOC 55, slow charge transfer at anode also influences the predominating mechanism [57].
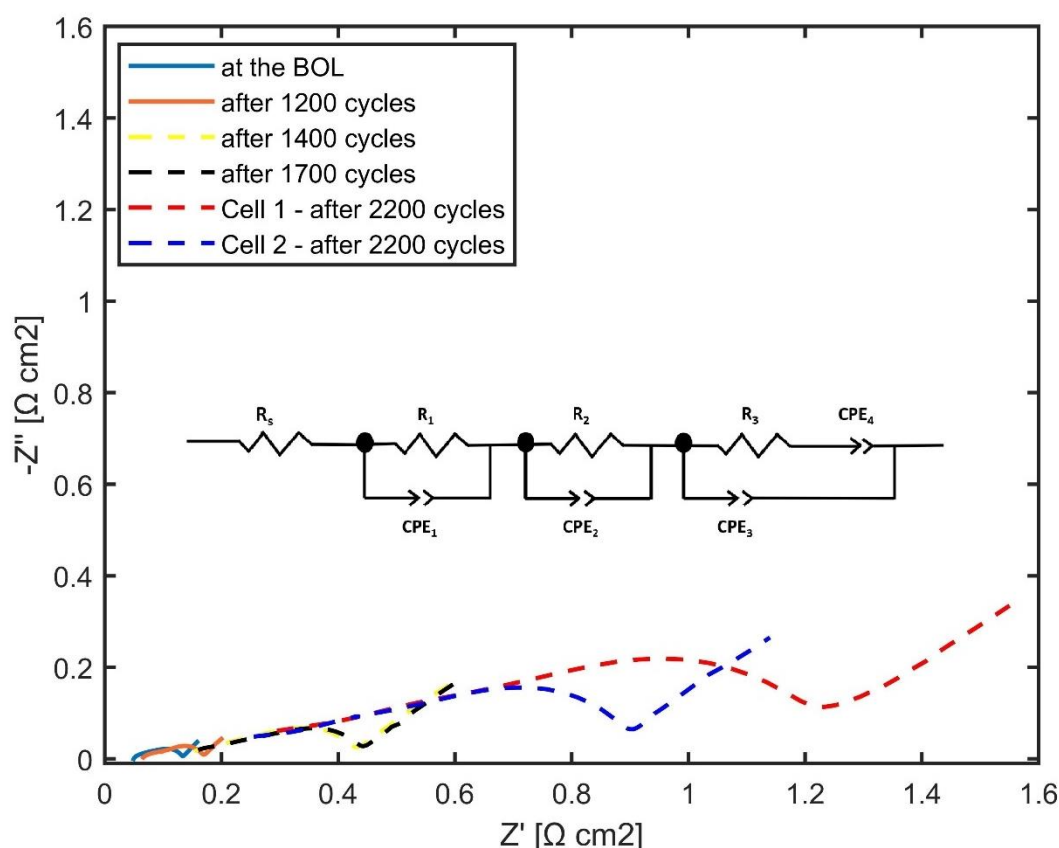
Figure 3 – Impedance variation during first life versus impedance rise during second life of LCO batteries. A solid line represents first life impedance. In contrast, a dashed line is used to represent the impedance of a Li-ion battery in its second life. Equivalent circuit fitted to the impedance data is also shown within.

Equivalent circuit parameters, estimated via data fitting using ZView proprietary software and shown in Table 3, confirm the dominance of charge transfer resistance in second life cells. Fig. 3 also shows that the EIS spectrum shifts towards the right side on the x-axis as the cells age, which is in line with the usual understanding of battery degradation behavior. Intersection of the impedance spectrum on the abscissa represents ohmic resistance, which is largely an indicator of electrolyte conductivity. The evident shift points towards reduced ionic conductivity owing to electrolyte degradation. This is a sign of SEI layer thickening. Additionally, there is a high probability of Li metal deposition on the anodes in second life batteries (F- and G- groups). Electrolyte solvent gets reduced upon encountering Li metal. This leads to irreversible consumption of the ion carriers and a decrease in electrolyte conductivity. Additionally, increase in ohmic resistance amplifies the polarization effects, visible in form of

capacity losses seen in Fig. 2. Diameter of the semicircle is expected to increase with the cycle count (aging). Here it is enlarged approximately 10 times that explains deteriorating performance of batteries during the second life operation. Increased diameter signifies increased charge transfer resistance due to loss of lithium inventory for reasons like decreased surface area and porosity due to film growth, and amplified electrolyte decomposition. It also infers probable loss of mechanical and electrical contact points for active material. A 10% volume expansion upon aging is quite normal for graphite anodes. However, repeated expansion-contraction causes pulverization or particle fracture, which has been previously cited as a reason for the increased impedance in batteries with graphitic anodes [58, 59]. Nevertheless, noteworthy is that the second life batteries at similar SOHs exhibited different impedance characteristics, which demands further investigation.

Cycles	R_s	R_1	CPE_1	R_2	CPE_2	R_3	CPE_3	CPE_4
BOL	0.048	0.049	0.139	0.009	0.007	0.038	0.680	105.000
1200	0.063	0.040	0.132	0.000	0.013	0.064	0.736	80.890
1400	0.142	0.143	0.161	0.053	0.020	0.082	0.280	19.000
1700	0.137	0.084	0.134	0.093	0.049	0.113	0.240	17.660
2200_1	0.194	0.170	0.037	0.287	0.024	0.580	0.170	9.454
2200_2	0.143	0.146	0.053	0.276	0.050	0.320	0.180	12.540

Table 3 – Parameters of the equivalent circuit fitted to the EIS curves of differently aged cells. R is resistance, C is capacitance and W is Warburg impedance. R_s represents ohmic resistance, Parallel circuit_1 depict interfacial impedance due to current collector, Parallel circuit_2 depict interfacial properties of the porous electrode, and Parallel circuit_3 depicts the charge transfer reactions, CPE denominates the constant phase element due to pseudo capacitance.

3.3. Physical changes in tested cells

Table 4 lists thickness measurements for the LCO full cells, aged differently. Photographs showing the measurements are offered in supporting information, Fig. S1. Pristine cells were approximately 5.1 mm thick and swelled to approximately 6.1 mm at the end of their first life (SOH 80%). The thickness became more than 8.6 mm during the second life use. A total change of roughly 69% in the thickness, and correspondingly volume, of these batteries was witnessed here. Out of this more than 71% occurred during the second life region. Despite this drastic

increase, aluminum packaging of all the second life cells remained intact; there were no discernable signs of any kind of venting and loss of mechanical integrity.

Category	Aging cycles	SOH (%)	Thickness (mm)
Pristine cell	0	100	5.14
First life cell	1200	78.6	6.14
Second life cells	1050	53.1	7.72
	950	52.17	7.85
	1200	39.96	8.0
	2200	18.92	8.5
	2200	19.72	8.56
	2200	18.0	8.63

Table 4 – Changes recorded in thickness of the LCO pouch cells due to aging

The large increase in cell thickness during second life cycling might cause problems if used in the typical commercial set-ups. E.g. BYD, a global EV manufacturer, maintains 0.5 – 1.0 mm intercellular spacing in its battery pack designs [60]. Larger gaps are known to promote layer delamination in pouch cells due to increased vibration transmission. Purpose of intercellular spacing is to minimize probability of cell-to-cell physical contact during an exothermic event such as thermal runaway. The air gap limits conductive heat transfer from failed cell/module to neighboring cells/modules and prevents the local event from taking a violent shape [61]. It is not designed to account for cell expansion due to aging. Space and volume availability are equally tight if not stricter in consumer devices and wearable electronic systems that mainly use LCO batteries. Furthermore, in view of the increasing compactness and miniaturization of end systems, swelling of cells is not permissible simply because there is no room to accommodate it in the packaging.

Swelling is a mark of gas generation during usage and storage. Gas evolution normally happens due to electrolyte reduction and is associated with SEI layer formation at anodes. Additionally, chemical transformation of Li_2CO_3 on the surface of the cathode material can lead to gas generation. Yongseon Kim determined the gas composition for LCO batteries as CO and CO_2 in a 60:40 mix [62, 63]. Validating it by comparing with the gas mixture composition from the

cells tested herein is out of scope of this work. Important point is that gassing causes non-negligible drop in Coulombic efficiency of battery cells. Excessive gassing over a longer period of usage is a major safety risk.

In LCO batteries, "free" lithium compounds available on cathode surface are sparse. Gas is, thus, produced mainly as a byproduct of electrolyte's reaction with delithiated LCO microstructure. Therefore, using electrolytes containing electron donating groups could be one way of suppressing their gassing tendency and, in doing so, ensuring their superior performance. E.g., cyclic structured carbonate solvents generate less gas than chain structured carbonate solvents, and their use instead can help. Another key point is that the volume of gas formed in LCO batteries increases linearly with passage of storage/usage time [62]. The same can be concluded to occur in our cells since their thickness increased linearly with usage time or number of cycles. It is because the generation mechanism is closely related to unavoidable LCO crystal structure transformation that happens due to aging. More details are presented in section 3.4.2. In contrast, surface reactions dominate the gas generation mechanism in NCA batteries. Consequentially, the volume of gas produced can be expected to decrease with time. Hence, we anticipate that they may be more suited to second life applications than the LCO batteries. Future work will verify this conjecture.

3.4. Postmortem analysis

Excessive swelling of these cells and the increased diameter of the semicircle in the Nyquist plots suggest pore clogging and evolution of electrode microstructure. There can be multiple reasons for it. These are investigated via post-mortem analysis, results of which are presented in the following text.

Fig. 4 presents photographs of different electrodes from the opened cells. LCO active material exhibited strong adherence onto the positive current collector in all cells. Some localized bright spots were identified in the second life batteries, sample image presented in Fig. 4f, otherwise

no macroscopic changes were determined without the need for special instruments. Severely aged cells illustrated changes in surface color distribution of the negative electrode and appearance of bluish or brownish grey patches in areas closer to the top and bottom edges. Patches were larger and more pronounced in electrodes from the F- and the G- groups. Additionally, some of these electrodes had silvery deposits (Fig. 4e). Color changes on the negative electrode have been reported by other groups as well [64-67]. On some occasions, unequal current density distribution caused by the tab placement and consequential difference in SEI character was considered responsible for this visual defect. On other instances, it was considered a reflection of trapped lithium inside graphite layer that somehow becomes electrically disconnected from the rest, i.e., can no longer participate in electrochemical reactions. There have been citations of gold color to various shades of red and orange owing to differences in graphite lithiation phases. On the other hand, blue has been previously ascribed to decomposition of organic product. In addition, we noticed that the aged graphite electrodes from the second life cells turned out to be significantly more brittle than the first life cell's electrodes. They felt noticeably susceptible to cracking. In fact, some cracks were already visible with bare eye near the folded section of the winding. Brittleness is most likely an outcome of binder disintegration. Consequentially, graphite powder and sometimes even larger chips fell off the electrode surface rather easily as the second life cells were unwound. As seen in the image (Fig. 4f), a lot of it is transferred on to the separator. This can potentially lead to loss of porosity in separator and, subsequently, to increased impedance. The observation matches to that of Xu et al. who evaluated the effect of SOH on the mechanical integrity of battery cells [68]. Their research showcases that decrease in SOH causes batteries to become structurally stiff and influences the failure stress significantly.

(a) SOH 100%

(b) SOH 78%

(c) SOH 52%

(d) SOH 38%

(e) SOH 40%

(f) SOH 18%

Figure 4 – (a) – (e) Photographs of graphite electrode from cells cycled different times, (f) photograph of disassembled cell G1 showing both the cathode and the anode along with the separator (in the middle). The separator looks extremely dirty as a lot of graphite has been transferred to it. Some graphite particles can be seen on the underlay as well, indicating highly reduced mechanical integrity of the electrode coatings.

3.4.1. Elemental changes over time

Changes in stability and chemical complexity of the LCO and graphite electrodes over time were evaluated through ICP-OES and AAS measurements. 5.5 – 6 mg/g of Li was detected on the representative pristine negative electrode samples. Still, the lithium to cobalt molar ratio (Li/Co) for the corresponding positive pristine samples was found to be more than 1.07. During the formation and the characterization cycles, some Li is irreversibly lost. Therefore, while using stoichiometric LCO, the Li/Co ratio is expected to be smaller than 1 after them. However, Li-ion batteries are typically manufactured with anode to cathode capacity ratio controlled to 1.1. This is to mitigate Li electroplating or dendrite formation over anode. Owing to this, extra Li must be added to the cathode material to ensure a good capacity after SEI formation on the 10% additional anode material. Hence, the finding confirming that the LCO cathodes examined in this study were Li-rich, to begin with, is expected. Comparison of the molar ratios for Li derived from the AAS results for the pristine cell # A3 and the second life cell # G3 reveal that 33.60 % of Li^+ were lost because of aging. Table 5(a) further points that the Li/Co ratio decreased as the battery cells aged. The accompanying data in Table 5(b) shows that the amount of Li on the anode increases with the cycle age of the sample. This confirms that most of the

Li lost from the cathode during cycling is in fact deposited on the graphite anode. The amount of Co detected on the graphite anode is low for all the aged samples, which indicates that Co dissolution on the positive electrode is diminutive. The ICP-OES also detected trace amounts of Al (< 0.0074 g/mol) in all the graphite samples, pristine included. No noticeable change is measured in the Al amount in the aged electrodes, suggesting that Al corrosion is not a problem either. The result indicates that active Li loss mechanism driven by continuous SEI build-up and electrolyte decomposition reaction is the primary cause for the observed capacity fade in the second life region.

Sample (POS)		Li (mg/mol)	Co (mg/mol)	Li/Co
ID	SOH (%)			
A3	100	9.94	8.82	1.13
A4	100	9.12	8.49	1.07
E1	86.965	7.81	8.63	0.91
E3	88.523	8.05	8.34	0.97
F3	39.967	7.67	10.08	0.76
F2	33.723	7.87	11.37	0.69
F1	32.018	6.73	10.04	0.67
G3	18.922	6.60	10.78	0.61

(a)

Sample (NEG)	A3	A4	E1	E3	F3	F2	F1	G3
Li (g/mol)	0.79	0.86	1.76	1.63	5.45	4.93	5.01	4.39

(b)

Table 5 – AAS and ICP-OES results for the selected cells from the test batch, (a) the positive electrode and (b) negative electrode samples

3.4.2. The phase composition of the materials

XRD data was used to obtain phase composition for each sample. The purpose of the analysis was to investigate what kind of structural changes occur at the positive electrode along cycling, and to obtain the lattice parameters to evaluate the amount of Li in the observed phases.

Especially the value of the c parameter is a strong indicator for a lost lithium from the ideal LCO structure.

The powder diffraction patterns were analyzed with the program FullProf [69], using mainly the LeBail profile fitting method but occasionally the structural model was also included in the fittings (*i.e.* the Rietveld method).

For the positive electrodes, several Li_xCoO_2 (x ≤ 1) phases and their mixtures were identified depending on the cycling conditions. Most of the analyzed materials are multiphased, at least to some extent. The phases present in this study are categorized into four stages (noted as H1-H3, M1) depending on the value of x in Li_xCoO_2, i.e., how much Li has extracted from the material. H notes for hexagonal structure and M for monoclinic. All structural models used in this work were adopted from [70], where the structural model for phase H3 is also predicted.

H1 refers to the classical $LiCoO_2$ phase (α-$NaFeO_2$ structure, number of formula units in the unit cell Z = 1), analyzed using a hexagonal unit cell with x_{Li} close to 1 and has a typical c-axis parameter of 14.05-14.08 Å. Composition for the H3 is ~$Li_{0.75}CoO_2$ and it has a superstructure (Z = 4), formed through Li/vacancy ordering from H1 [70]. Typical c length in H3 is estimated to be 14.19-14.22 Å. H2 is classified in our study as a transition phase from H1 to H3, thus not properly defined in terms of crystal structure. For H2, the c values seem to vary between 14.12-14.17 Å. The reason for this classification of phases is ascribed to the values of the observed extended lattice. The values do not yet match for the distorted H3 phase with a superstructure but are unconvincingly high to originate only from the coulombic interactions that enlarge the c axis when Li is lost from the structure. Finally, a monoclinic structure, M1, with a composition of $Li_{0.5}CoO_2$ is found in extensively cycled samples. M1 experiences major structural changes, thus the lattice parameters are no longer comparable to hexagonal phases as such.
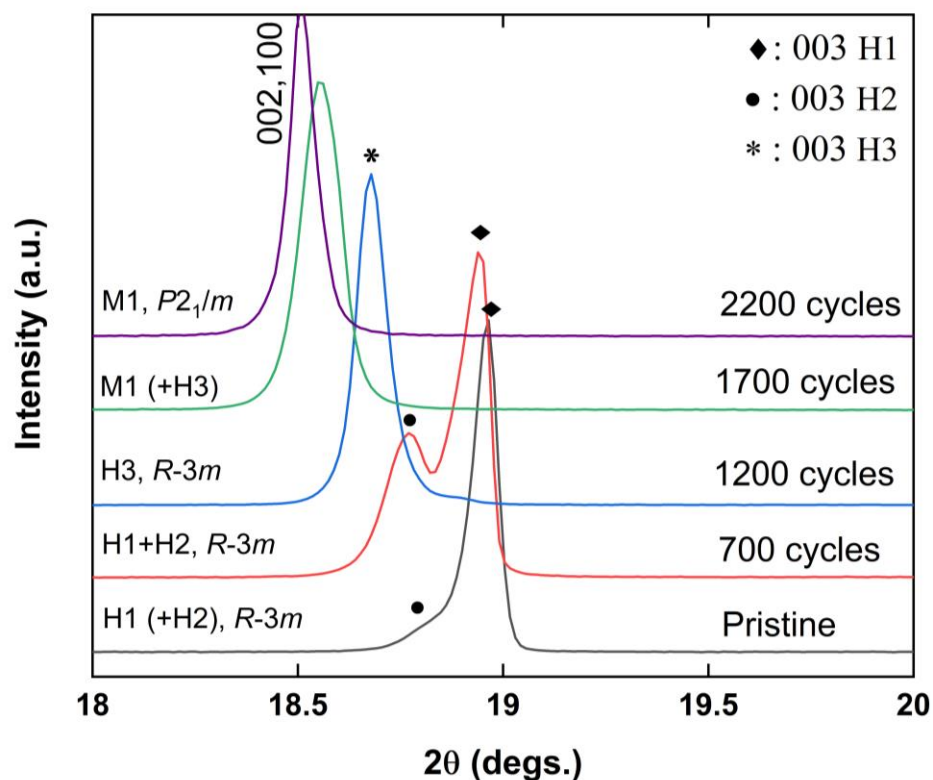
Figure 5 – A zoom of the normalized XRD patterns for selective positive electrodes with representative cycling conditions (see text for structure description). The phase evolution can be evidenced through changes in the position of 003 reflection, determinative for the lattice parameter c. The same phenomenon can be seen at higher angles through secondary reflection effect (not shown here).

Fig. 5 shows the observed phase evolution in XRD for representative samples upon aging using the notation used in the present work, presented as a magnification of the most intensive Bragg reflections in the measured XRD patterns. R-$3m$ and $P2_1/m$ are the precise space groups used in the analyses, and the 003 Miller index (hkl system) accompanied by its gradual shift to left is an indicator of the increasing value of lattice parameter c.

As the indicative supercell reflections for H3 (and possibly H2) are not actually visible by laboratory X-ray diffraction energy, the H1-H3 phases were distinguished from each other based on the extracted lattice parameter value c_H and somewhat by the shapes of the Bragg reflections (*i.e.*, full-width at half maximum, FWHM).

The compositions of the identified phases in the samples were estimated from their c parameters as follows: x = 1-0.94 (H1, a_H x a_H x c_{H1}), x = 0.93-0.75 (H2), x ≈ 0.75 (H3, $2a_H$ x

$2a_H$ x c_{H3},) and x ≈ 0.5 (M1, $\sqrt{3}a_H$ x a_H x $2\sqrt{3}a_H$, β ~99.6°). As a conclusion, the XRD results clearly indicate how Li is gradually extracted from the positive electrode material along increasing amount of cycles and finally undergoes a major structural transition from hexagonal to monoclinic symmetry, as shown in previous studies as well, e.g. [71, 72].

A complete fit of an example XRD pattern using the Rietveld method to extract the lattice parameters is shown in the Supplementary information (Fig. S2.)

3.4.3. Changes in Particle Morphology
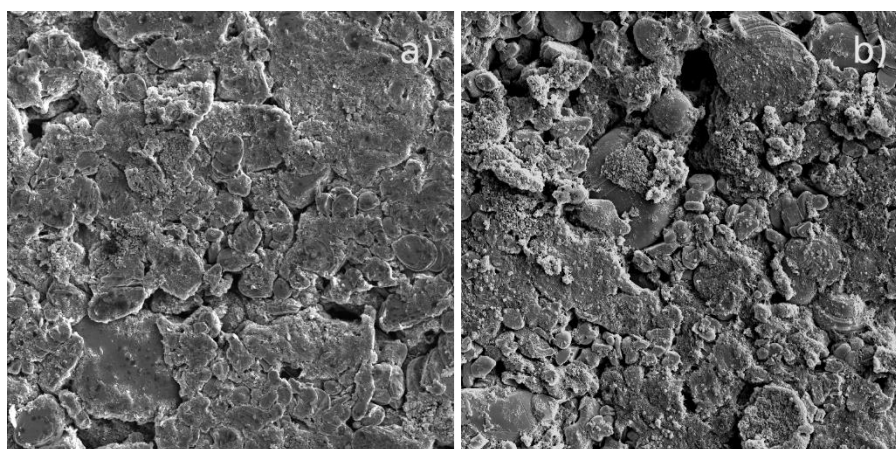
Figure 6 – Representative SEM images of the LCO positive electrodes at different stages of aging with 5kx magnification. a) pristine cell, b) 20% of the initial capacity remaining.
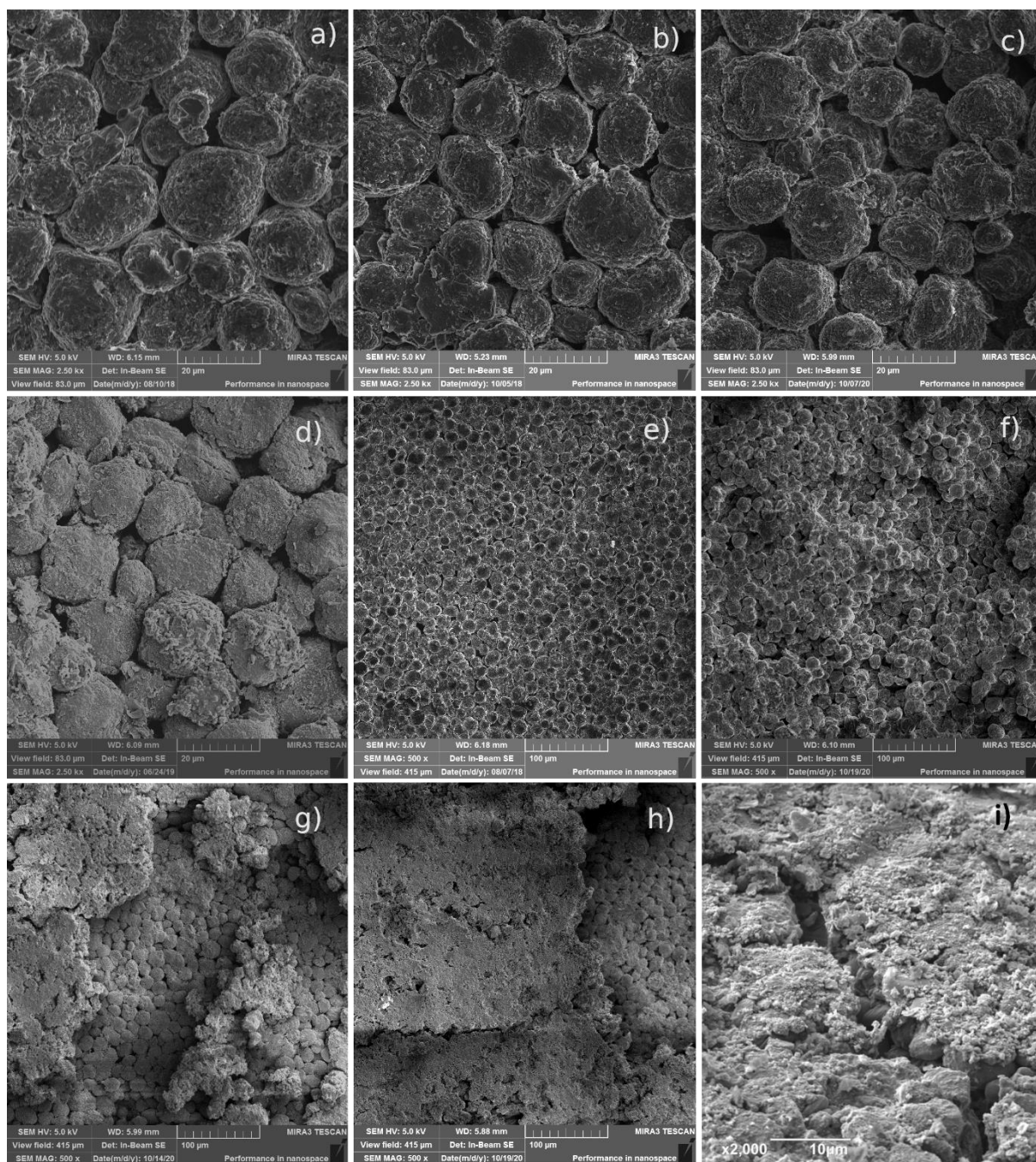
Figure 7 – Representative SEM images of the graphite negative electrodes at different stages of aging. a) pristine cell, b) 89%, c) 52%, d) 34% with 2.5kx magnification, e) pristine, f) 89%, g) 52%, h) 34% with 500x magnification and i) a crack in the graphite coating dividing it, literally, into two parts.

The morphology of the electrodes in the investigated cells was analyzed with SEM. The micrographs of the positive and negative electrodes at different stages of cycling are presented in Fig. 6 and Fig. 7, respectively. The shape of $LiCoO_2$ particles varies from oval to slightly angular. Their size varies between 1-10 µm with the average of 4 µm and standard variation of

2.5 µm. No change in the particle size is observed upon aging. The electrodes stay mostly intact through long-term cycling. Some small loosening of particles on the surface of the electrode is observed. Fig. 7 displays spherical or oval shaped graphite particles with the average size being averagely 14 µm in diameter with standard deviation of 2.2 µm. Their size also remains the same upon aging. Similarly, to positive electrodes, loosening of the particles during the cycling is observed in the graphite electrodes as well. The loosening, however, is more severe and the changes are clearly visible already at SOH 89%. The lower the SOH is, the more severe the loosening becomes. In addition, with closer inspection, fine cracks are observed in the particles aged to SOH 40% or further. The morphology of the particle surface also smoothens upon aging. The loosening of the particles and the cracking are attributed to volume changes and mechanical stress in the active material upon charge and discharge. The surface smoothening is attributed to the thickening of the SEI layer.

In addition, with prolonged aging, a thick surface layer is observed, with patches of unchanged graphite visible under it. The first patches of this layer are observed already at SOH 90% but they become larger with continued cycling. With closer inspection, the layer seems to be formed of decomposed graphite particles. The EDX measurements show that the layer contains mainly carbon and oxygen. They are presented in supporting information, Fig. S3. Therefore, we believe this layer is formed of loosened graphite particles that after mostly detaching from the surface have decomposed with continued cycling. There are two possible explanations for the patch-like structure of the surface film. First, as seen in Fig. 7f, the graphite loosening does not occur evenly on the surface but in ridges and clusters. This could lead to uneven formation of the surface film. Second, during the cell disassembly, some of the graphite electrode got stuck to the removed separator. Some of the holes, in which the smooth graphite is visible, could have formed this way. The high oxygen content in the surface film is explained by the

sample preparation process, as the samples were exposed to air between the cell disassembly and the SEM measurements.

3.4.3.1. Site-specific changes

Fig. 8a presents top view FIB-SEM image of the graphite coating from a second life cell. Many particles are seen with cracks, indicated with red arrows. Cross-sectional micrographs in Fig. 8b to 8d disclosed presence of large internal cracks and voids. Some finer microcracks are also visible that may be considered in early stages of crack growth phase. The vertical pillar like features seen in the cross-sectional images, namely Fig. 8d, are graphic artefacts from milling operation; otherwise, no impression of any SEI film on the edges of these internal cracks is available from these images. One explanation for the non-existing SEI film could be "inadequate" electrolyte wetting. Electrolyte wetting is essential to the SEI layer formation. However, a large portion of intrinsic pores can remain unwetted even after using vacuum assist in classical battery manufacturing process [73, 74]. Regardless, the theory can be refuted herein because a thick surface layer is clearly visible on the outermost edges of the same particles. A logical conclusion, therefore, would be to treat the inner cracks as closed pores that do not contribute to surface area available for electrochemical reaction or influence the ionic and electronic transport within the system. Another observation relates to the thickness of the SEI film. The zoomed-in cross sectional image confirms that the SEI layer thickness in the second life cells varies from 89 nm to 711 nm. A sufficiently thick SEI layer is needed to prevent continuous electrode passivation. However, the Li-ions must be able to diffuse through this layer for the electrochemical reactions to proceed. Increasing SEI layer thickness leads to an increase in cell impedance and a corresponding square-root of time shaped degradation profile, seen in Fig. 2a.
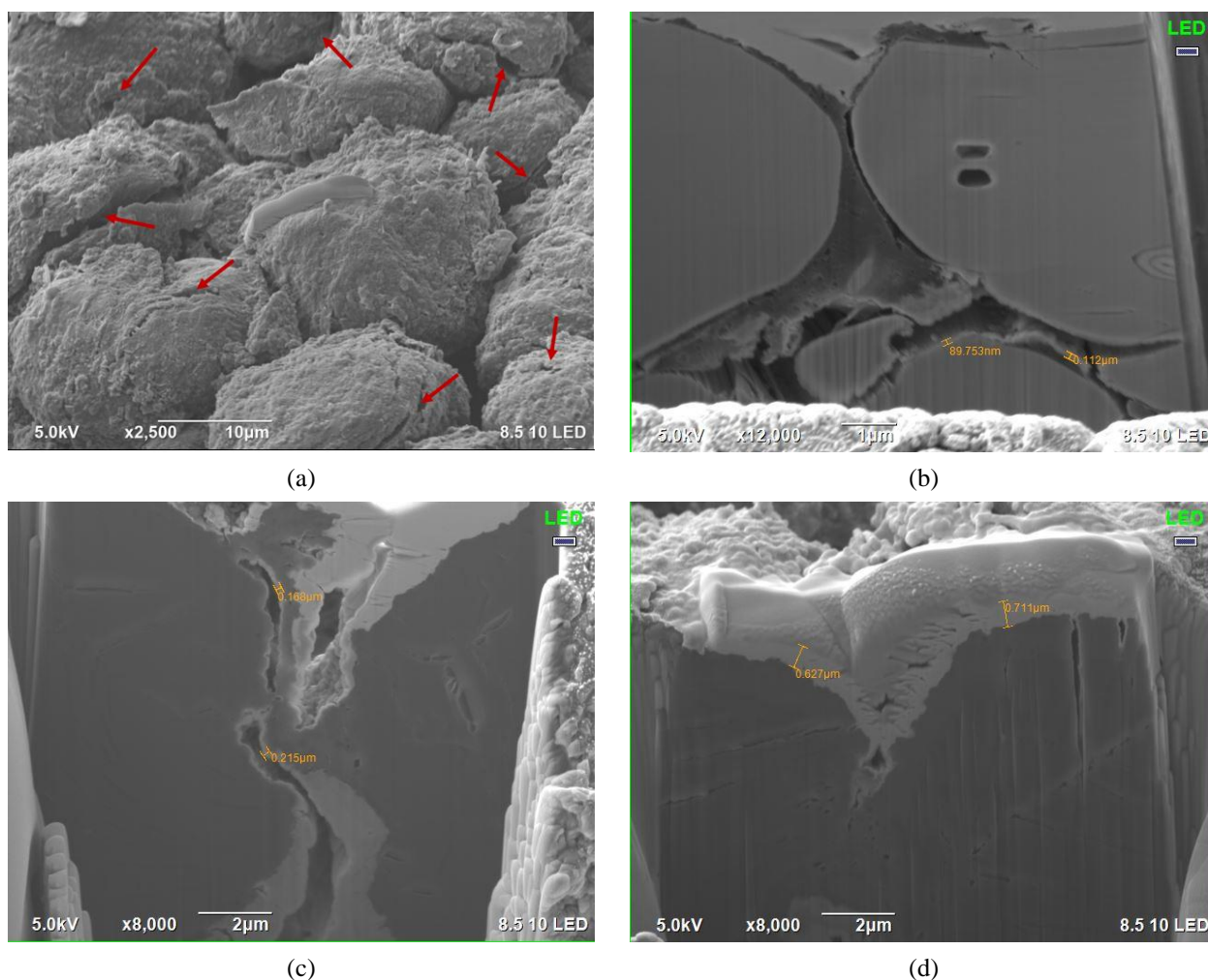
Figure 8 – (a) SEM image showing a graphite anode from a second life cell. The particles have surface cracks that are marked with red arrows, (b) – (d) cross-sectional FIB-SEM image of graphite coatings from different cells showing internal cracks and a surface layer of varying thicknesses

3.4.4. Half-cell study

LCO/Li and graphite/Li half-cell measurements were used to gather more information about the observed capacity fade. As the full cells were fully discharged before disassembly, the electrodes used in the half-cells were assumed to be fully discharged. The assumption was validated through a slow galvanostatic discharge test at 0.05C. Expectedly, none of the half-cells illustrated any measurable residual capacity confirming that the pre-disassembly discharge step indeed fully discharged the cells. Thereafter, the loss of cyclable Li was estimated by charging the half-cell and measuring its discharge capacity.

Discharge capacities measured for the three cycles for the graphite half-cells (negative electrode) and the LCO half-cells (positive electrode) are presented in Table 6. The average capacity for each cycle is presented as well, and they are used in the comparison between different cell groups. A plain look at various capacities listed in it confirm that the full cells tested here were Li-rich cells. Positive Electrode to Negative Electrode ratio ($Avg\_pristine$) for the third cycle is 123.31%. This is several percent more than the Li/Co ratio determined for the pristine positive electrodes through the AAS/ICP-OES analysis. Lesser values for the full cells could be because some cyclable Li^+ is lost to the negative electrode during the SEI formation step. However, the Li metal counter foil compensates this loss in the cathode half-cells during the initial lithiation steps. Further, the half-cells in each group demonstrated more stable capacities in comparison to the originating full cells. That is, the cell-to-cell variation seen particularly in the F- and G- group half-cell capacities (in Table 6) seem less relative to the difference in the F- and G- group full cell capacities (in Table 2). This could potentially be due to the different electrolyte used and the amount of electrolyte filed in the half-cells than in the commercial cells. In addition, different cycling current and SEI film of different composition due to the different electrolyte could have played a role in reducing the cell variability as well.

Half-cell – Base electrode	NE - Discharge Capacity (mAh)			PE - Discharge Capacity (mAh)		
	1st Cycle	2nd Cycle	3rd Cycle	1st Cycle	2nd Cycle	3rd Cycle
A1	4.244	4.25	4.246	5.292	5.276	5.292
A2	4.182	4.21	4.292	5.276	5.339	5.335
A3	4.277	4.253	4.254	5.171	5.15	5.149
Avg_Pristine	**4.234**	**4.237**	**4.264**	**5.246**	**5.255**	**5.258**
E1	3.947	3.964	3.973	4.834	4.838	4.826
E2	3.935	3.993	3.998	4.847	4.743	4.732
E3	3.897	3.895	3.893	4.702	4.702	4.704
Avg_FL	**3.926**	**3.951**	**3.955**	**4.794**	**4.761**	**4.754**
F1	3.56	3.568	3.552	4.139	4.291	4.351
F2	3.499	3.483	3.479	3.988	3.945	3.856

F3	3.321	3.355	3.363	4.042	4.193	4.147
Avg_SL	**3.46**	**3.469**	**3.464**	**4.056**	**4.143**	**4.118**
G1	2.79	2.95	2.922	3.491	3.400	3.299
G2	3.204	2.919	2.83	3.660	3.615	3.546
G3	2.964	3.075	3.103	3.57	3.577	3.574
Avg_ESL	**2.982**	**2.981**	**2.952**	**3.574**	**3.531**	**3.473**

Table 6 – Discharge capacities measured during cycles 1-3 for the half-cells with the pristine and differently aged working electrodes. Cycling currents of 0.12 mAh and 0.15 mAh used for the negative and positive half cells, respectively. (NE = Negative or graphite electrode; PE = Positive or LCO electrode; FL = first life cells; SL = second life cells; ESL = extended second life cells)

Nevertheless, the major observation relates to a significant drop in the discharge capacity for both the G - group electrodes in comparison to the pristine ones – 30.7% and 33.94% to be exact for the negative and positive electrodes, respectively. Although, the decreased amount is very similar to the Li^+ loss estimated for the positive electrodes from the AAS/ICP-OES results (33.60 %), it represents the loss of active material at the two electrodes. As discussed previously in context of the XRD results, the active material loss accompanied with the phase transformation of the bulk structure is mainly responsible for the positive electrode aging. In contrast, particle micro-cracking and binder disintegration leading to isolation and loss of electrical contact are the two major causes for the capacity decay of the negative electrode. Based on this analysis, a large portion of the unrecoverable capacity for the second life cells can be predominantly attributed to the loss of the active material at the two electrodes. The remaining is a result of decrease in Li inventory owing to intensified electrolyte decomposition and subsequent SEI layer build-up.

4. Conclusion

Electric cords represent a form of restriction that the society is trying to break away from. Consequentially, battery-powered devices of all kinds are the new norm. Therefore, Li-ion battery degradation modes and mechanism have received a lot of attention in recent years, but the past research did not investigate battery behaviour beyond SOH 80%. Moreover, a lack of

standards and regulations governing consumer appliances market mean that a large percentage of it can be "non-certified" or untested items. Performance of used battery systems can therefore significantly vary. To top this up, consumer appliances do not generally showcase battery's SOH. This can create a major safety risk for the users as they may not realise when they have reached the safety limit. To alleviate some of the concern, this paper focuses on the second or extended life (SOH $\leq$ 80%) of Li-ion batteries of chemistry that is common in consumer applications.

Accordingly, galvanostatic cycle life tests well beyond the usual cut-off of SOH 80% were conducted in room temperature environment using higher charge/discharge currents than those used by the manufacturer in standard testing. Some cells were calendar aged as well. The shortest first life measured was 1.8 times the cycle life listed in the cell's technical specification sheet. Further, we recorded a marginal intercellular variability at SOHs > 80% that grew rapidly in the second life region. Substantial increase in charge transfer resistance of the electrodes is estimated to be the reason behind the exhibited behaviour. One silver lining is that despite the strenuous circumstances, no sudden death or extreme failure events were observed, which indicates towards acceptable manufacturing quality of the state-of-the-art commercial LCO cells. Nevertheless, in terms of number of cycles for the second life cells, 300 to 400 aging cycles on average could easily be the difference between the two cells at same SOH. Therefore, frequent sorting is recommended to maximise system performance during second life applications. Also, gas generation and the subsequent increase in volume of the second life cells needs to be better managed as it can be a major problem in applications where compact packaging is a non-negotiable requirement.

Acknowledgement

Supporting Information

(a) Pristine cell (SOH 100)

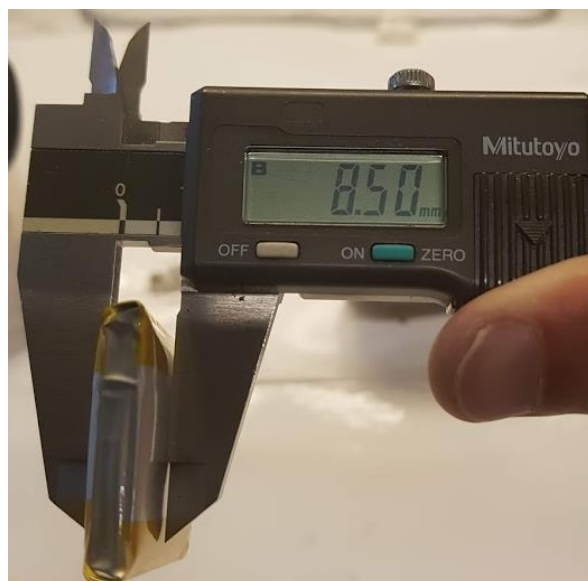
(b) Cycled 1200 times (SOH 78.6)

(c) Cycled 1050 times (SOH 53.1)

(d) Cycled 950 times (SOH 52.17)

(e) Cycled 1200 times (SOH 39.96)

(f) Cycled 2200 times (SOH 18.92)

(g) Cycled 2200 times (SOH 19.72)

(h) Cycled 2200 times (SOH 18.00)

Figure S1 – Comparative evaluation of the physical change (expansion in thickness) in the cycled cell exiting the test matrix relative to that the pristine LCO battery cell
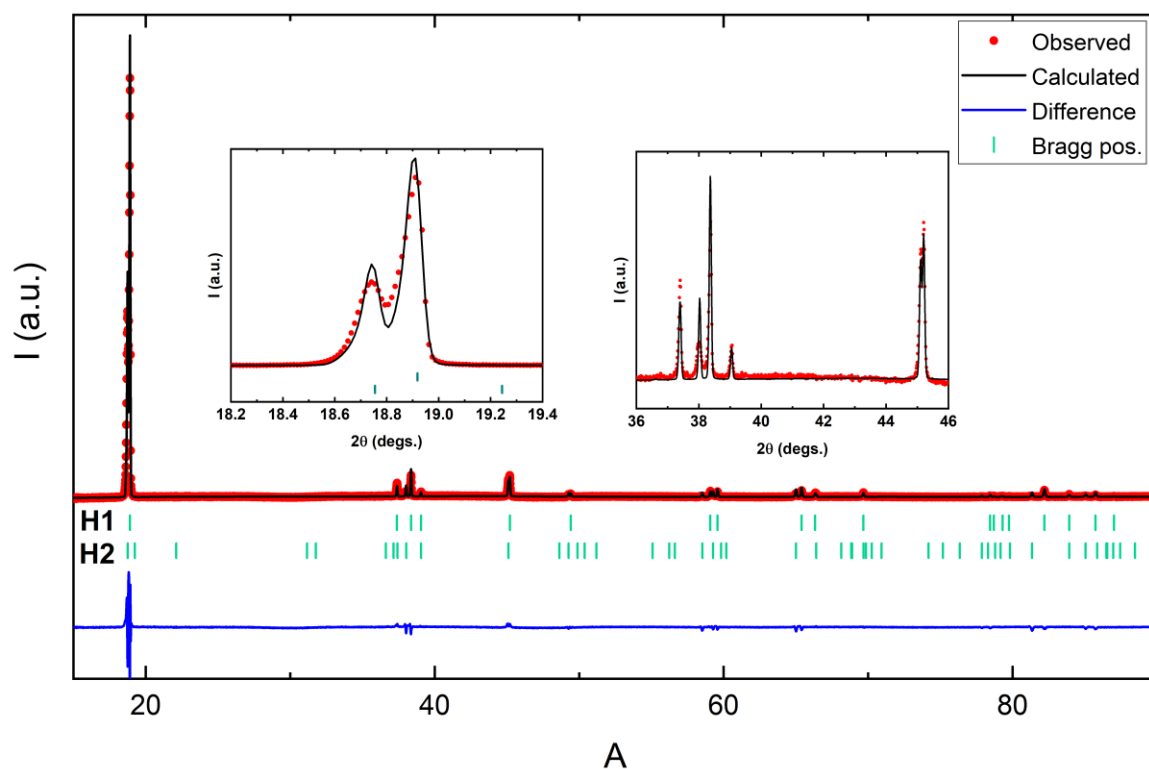
Figure S2 – Example of a two-phase Rietveld refinement for 700 cycles. The two-phased sample was fitted best using the phases H1 and H2, the latter labeled based on the *c*-axis length. All the samples showed significant 00*l* orientation (abnormally high intensity of the 00l reflections), which was fitted using the March-Dollase function.
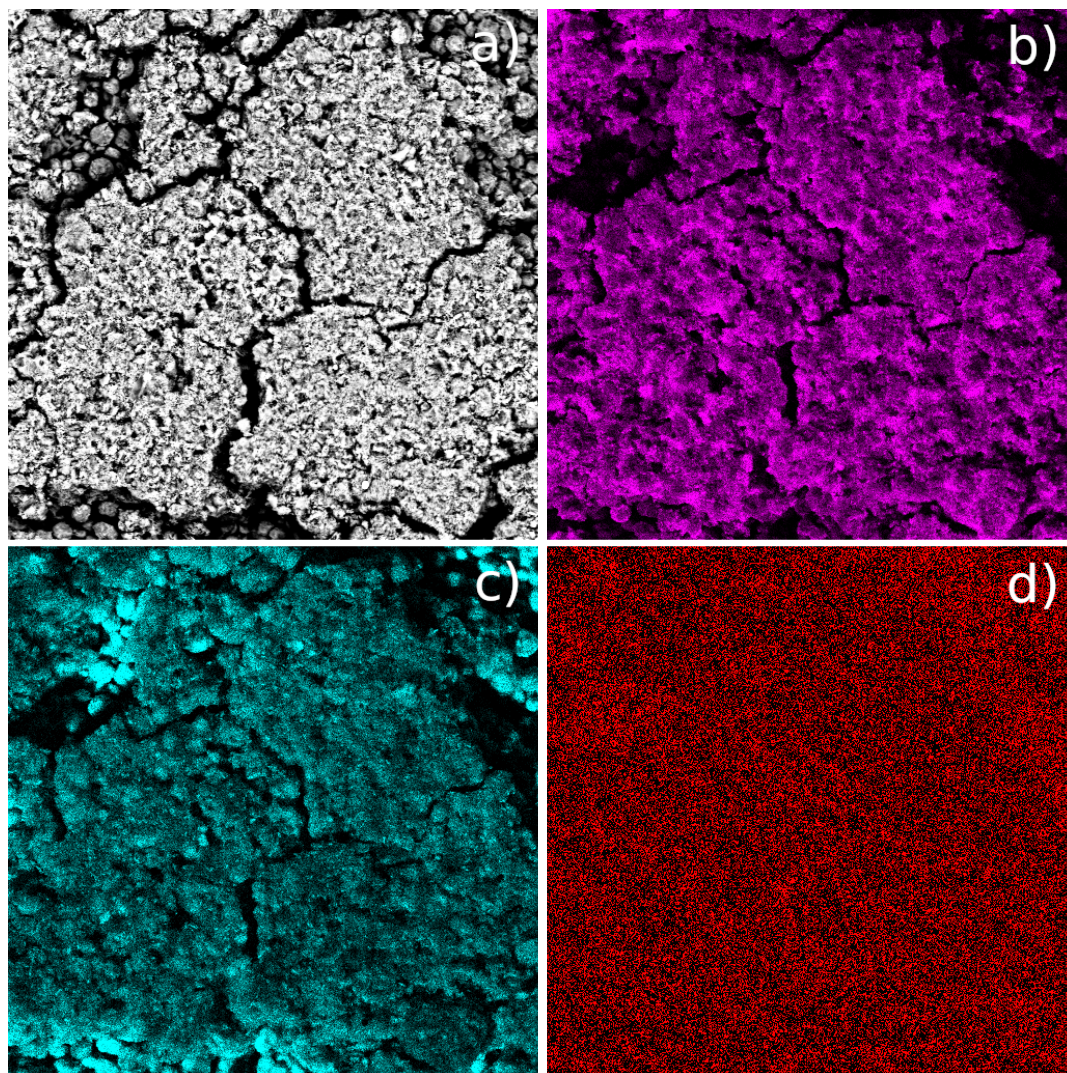
Figure S3 – EDS maps for graphite electrode aged to 78% of the initial capacity. a) the surface layer of the electrode with 500x magnification, b) oxygen distribution, c) carbon distribution and d) Cu distribution.

References

1. Duraisamy, E., S. Archana, A. Prasath, and P. Elumalai, High Capacity and High Stability Lithium-Ion Battery Using Nano Sn/Sns-Decorated Carbon Leaf Anode and Licoo2 Cathode for Consumer Electronics Electrochimica Acta, 2020. **338**: p. 135863.
2. Liu, X., K. Zhao, Z.L. Wang, and Y. Yang, Unity Convoluted Design of Solid Li-Ion Battery and Triboelectric Nanogenerator for Self-Powered Wearable Electronics Advanced Energy Materials, 2017. **7**(22): p. 1701629.
3. Wang, Y., C. Chen, H. Xie, T. Gao, Y. Yao, G. Pastel, X. Han, Y. Li, J. Zhao, and K. Fu, 3d-Printed All-Fiber Li-Ion Battery toward Wearable Energy Storage Advanced Functional Materials, 2017. **27**(43): p. 1703140.
4. Kulkarni, A.; Kapoor, A.; Arora, S. *Battery Packaging and System Design for an Electric Vehicle*; SAE Technical Paper 2015-01-0063; SAE International: Melbourne, Australia, 2015.
5. Arora, S., K. Tammi, and P. Sainio, Cycle Life Assessment of Commercial Cells with Ni-Rich Cathode and Si-Graphite Anode: Are Advanced Batteries for Real? ECS Meeting Abstracts, 2020. **MA2020-02**(2): p. 457-.
6. Schmidt, A., A. Smith, and H. Ehrenberg, Power Capability and Cyclic Aging of Commercial, High Power Lithium Ion Battery Cells with Respect to Different Cell Designs Journal of Power Sources, 2019. **425**: p. 27-38.
7. Arora, S., A. Kapoor, and W. Shen, Application of Robust Design Methodology to Battery Packs for Electric Vehicles: Identification of Critical Technical Requirements for Modular Architecture Batteries, 2018. **4**(3): p. 30.
8. Arora, S.; Shen, W.; Kapoor, A. *Designing a Robust Battery Pack for Electric Vehicles Using a Modified Parameter Diagram*; SAE Technical Paper 2015-01-0041; SAE International: Melbourne, Australia, 2015
9. Huotari, M., S. Arora, A. Malhi, and K. Främling, Comparing Seven Methods for State-of-Health Time Series Prediction for the Lithium-Ion Battery Packs of Forklifts Applied Soft Computing, 2021. **111**: p. 107670.
10. Arora, S., W. Shen, and A. Kapoor, Review of Mechanical Design and Strategic Placement Technique of a Robust Battery Pack for Electric Vehicles Renewable and Sustainable Energy Reviews, 2016. **60**: p. 1319-31.
11. Arora, S., A.T. Abkenar, S.G. Jayasinghe, and K. Tammi, *Chapter 1 - Heavy-Duty Electric Vehicles and Society*, in *Heavy-Duty Electric Vehicles*, S. Arora, A.T. Abkenar, S.G. Jayasinghe, and K. Tammi, Editors. 2021, Butterworth-Heinemann. p. 1-34.
12. Huotari, M., S. Arora, A. Malhi, and K. Främling. *A Dynamic Battery State-of-Health Forecasting Model for Electric Trucks: Li-Ion Batteries Case-Study*. in *ASME 2020 International Mechanical Engineering Congress and Exposition*. 2020.
13. Arora, S. and A. Kapoor, Experimental Study of Heat Generation Rate During Discharge of Lifepo4 Pouch Cells of Different Nominal Capacities and Thickness Batteries, 2019. **5**(4): p. 70.
14. Arora, S., A. Kapoor, and W. Shen, A Novel Thermal Management System for Improving Discharge/Charge Performance of Li-Ion Battery Packs under Abuse Journal of Power Sources, 2018. **378**: p. 759-75.
15. Arora, S. *Design of a Modular Battery Pack for Electric Vehicles*. Ph.D. Thesis, Swinburne University of Technology, Melbourne, Australia, 2017.
16. Arora, S. and W. Shen, Advances in Rechargeable Lithium Ion Batteries and Their Systems for Electric and Hybrid Electric Vehicles Rechargeable Lithium-Ion Batteries: Trends and Progress in Electric Vehicles, 2020. **3**: p. 99.
17. Hunt, G., Usabc Electric Vehicle Battery Test Procedures Manual Washington, DC, USA: United States Department of Energy, 1996.
18. Doughty, D.H. and E.P. Roth, A General Discussion of Li Ion Battery Safety The Electrochemical Society Interface, 2012. **21**(2): p. 37.

19. Nitta, N., F. Wu, J.T. Lee, and G. Yushin, Li-Ion Battery Materials: Present and Future Materials Today, 2015. **18**(5): p. 252-64.

20. Reimers, J.N. and J. Dahn, Electrochemical and in Situ X-Ray Diffraction Studies of Lithium Intercalation in Li X Coo2 Journal of the Electrochemical Society, 1992. **139**(8): p. 2091.

21. Zhang, S.S., The Effect of the Charging Protocol on the Cycle Life of a Li-Ion Battery Journal of Power Sources, 2006. **161**(2): p. 1385-91.

22. Guan, T., P. Zuo, S. Sun, C. Du, L. Zhang, Y. Cui, L. Yang, Y. Gao, G. Yin, and F. Wang, Degradation Mechanism of Licoo2/Mesocarbon Microbeads Battery Based on Accelerated Aging Tests Journal of Power Sources, 2014. **268**: p. 816-23.

23. Barcellona, S. and L. Piegari, Effect of Current on Cycle Aging of Lithium Ion Batteries Journal of Energy Storage, 2020. **29**: p. 101310.

24. Zhang, L., J. Jiang, and W. Zhang, Capacity Decay Mechanism of the Lco + Nmc532/Graphite Cells Combined with Post-Mortem Technique Energies, 2017. **10**(8): p. 1147.

25. Roth, E.P. and D.H. Doughty, Thermal Abuse Performance of High-Power 18650 Li-Ion Cells Journal of Power Sources, 2004. **128**(2): p. 308-18.

26. Larsson, F., S. Bertilsson, M. Furlani, I. Albinsson, and B.-E. Mellander, Gas Explosions and Thermal Runaways During External Heating Abuse of Commercial Lithium-Ion Graphite-Licoo2 Cells at Different Levels of Ageing Journal of Power Sources, 2018. **373**: p. 220-31.

27. Richter, F., P.J. Vie, S. Kjelstrup, and O.S. Burheim, Measurements of Ageing and Thermal Conductivity in a Secondary Nmc-Hard Carbon Li-Ion Battery and the Impact on Internal Temperature Profiles Electrochimica Acta, 2017. **250**: p. 228-37.

28. Vetter, J., P. Novák, M.R. Wagner, C. Veit, K.-C. Möller, J. Besenhard, M. Winter, M. Wohlfahrt-Mehrens, C. Vogler, and A. Hammouche, Ageing Mechanisms in Lithium-Ion Batteries Journal of power sources, 2005. **147**(1-2): p. 269-81.

29. Hausbrand, R., G. Cherkashinin, H. Ehrenberg, M. Gröting, K. Albe, C. Hess, and W. Jaegermann, Fundamental Degradation Mechanisms of Layered Oxide Li-Ion Battery Cathode Materials: Methodology, Insights and Novel Approaches Materials Science and Engineering: B, 2015. **192**: p. 3-25.

30. Yan, P., L. Xiao, J. Zheng, Y. Zhou, Y. He, X. Zu, S.X. Mao, J. Xiao, F. Gao, and J.-G. Zhang, Probing the Degradation Mechanism of Li2mno3 Cathode for Li-Ion Batteries Chemistry of Materials, 2015. **27**(3): p. 975-82.

31. Zhang, S.S., Unveiling Capacity Degradation Mechanism of Li-Ion Battery in Fast-Charging Process ChemElectroChem, 2020. **7**(2): p. 555-60.

32. Park, K.-J., J.-Y. Hwang, H.-H. Ryu, F. Maglia, S.-J. Kim, P. Lamp, C.S. Yoon, and Y.-K. Sun, Degradation Mechanism of Ni-Enriched Nca Cathode for Lithium Batteries: Are Microcracks Really Critical? ACS Energy Letters, 2019. **4**(6): p. 1394-400.

33. Keil, P. and A. Jossen, Calendar Aging of Nca Lithium-Ion Batteries Investigated by Differential Voltage Analysis and Coulomb Tracking Journal of The Electrochemical Society, 2016. **164**(1): p. A6066.

34. Muto, S., K. Tatsumi, Y. Kojima, H. Oka, H. Kondo, K. Horibuchi, and Y. Ukyo, Effect of Mg-Doping on the Degradation of Linio2-Based Cathode Materials by Combined Spectroscopic Methods Journal of Power Sources, 2012. **205**: p. 449-55.

35. Genieser, R., S. Ferrari, M. Loveridge, S. Beattie, R. Beanland, H. Amari, G. West, and R. Bhagat, Lithium Ion Batteries (Nmc/Graphite) Cycling at 80 C: Different Electrolytes and Related Degradation Mechanism Journal of Power Sources, 2018. **373**: p. 172-83.

36. Li, X., A.M. Colclasure, D.P. Finegan, D. Ren, Y. Shi, X. Feng, L. Cao, Y. Yang, and K. Smith, Degradation Mechanisms of High Capacity 18650 Cells Containing Si-Graphite Anode and Nickel-Rich Nmc Cathode Electrochimica Acta, 2019. **297**: p. 1109-20.

37. Li, T., X.-Z. Yuan, L. Zhang, D. Song, K. Shi, and C. Bock, Degradation Mechanisms and Mitigation Strategies of Nickel-Rich Nmc-Based Lithium-Ion Batteries Electrochemical Energy Reviews, 2020. **3**(1): p. 43-80.

38.   Pan, B., D. Dong, J. Wang, J. Nie, S. Liu, Y. Cao, and Y. Jiang, Aging Mechanism Diagnosis of Lithium Ion Battery by Open Circuit Voltage Analysis Electrochimica Acta, 2020. **362**: p. 137101.

39.   Panchal, S., J. Mcgrory, J. Kong, R. Fraser, M. Fowler, I. Dincer, and M. Agelin-Chaab, Cycling Degradation Testing and Analysis of a Lifepo4 Battery at Actual Conditions International Journal of Energy Research, 2017. **41**(15): p. 2565-75.

40.   Zhang, Y., C.-Y. Wang, and X. Tang, Cycling Degradation of an Automotive Lifepo4 Lithium-Ion Battery Journal of power sources, 2011. **196**(3): p. 1513-20.

41.   EuropeanCommission, *Proposal for a Regulation of the European Parliament and of the Council Concerning Batteries and Waste Batteries, Repealing Directive 2006/66/Ec and Amending Regulation (Eu) No 2019/1020*, in *2020/0353(COD)*, T.E. PARLIAMENT, Editor. 2020: Brussels.

42.   Klett, M., R. Eriksson, J. Groot, P. Svens, K. Ciosek Högström, R.W. Lindström, H. Berg, T. Gustafson, G. Lindbergh, and K. Edström, Non-Uniform Aging of Cycled Commercial Lifepo4//Graphite Cylindrical Cells Revealed by Post-Mortem Analysis Journal of Power Sources, 2014. **257**: p. 126-37.

43.   Arora, S., A.T. Abkenar, S.G. Jayasinghe, and K. Tammi, *Chapter 8 - Battery Management System: Charge Balancing and Temperature Control*, in *Heavy-Duty Electric Vehicles*, S. Arora, A.T. Abkenar, S.G. Jayasinghe, and K. Tammi, Editors. 2021, Butterworth-Heinemann. p. 173-203.

44.   Ramadass, P., B. Haran, R. White, and B.N. Popov, Capacity Fade of Sony 18650 Cells Cycled at Elevated Temperatures: Part I. Cycling Performance Journal of Power Sources, 2002. **112**(2): p. 606-13.

45.   Arora, S., A.T. Abkenar, S.G. Jayasinghe, and K. Tammi, *Chapter 4 - Materials and Manufacturing Methods for Advanced Li-Ion Batteries*, in *Heavy-Duty Electric Vehicles*, S. Arora, A.T. Abkenar, S.G. Jayasinghe, and K. Tammi, Editors. 2021, Butterworth-Heinemann. p. 69-104.

46.   Scott, I.D., Y.S. Jung, A.S. Cavanagh, Y. Yan, A.C. Dillon, S.M. George, and S.-H. Lee, Ultrathin Coatings on Nano-Licoo2 for Li-Ion Vehicular Applications Nano letters, 2011. **11**(2): p. 414-8.

47.   Xie, J., J. Zhao, Y. Liu, H. Wang, C. Liu, T. Wu, P.-C. Hsu, D. Lin, Y. Jin, and Y. Cui, Engineering the Surface of Licoo 2 Electrodes Using Atomic Layer Deposition for Stable High-Voltage Lithium Ion Batteries Nano Research, 2017. **10**(11): p. 3754-64.

48.   Arora, S., A.T. Abkenar, S.G. Jayasinghe, and K. Tammi, *Heavy-Duty Electric Vehicles: From Concept to Reality*. 2021: Elsevier.

49.   Chen, H. and J. Shen, A Degradation-Based Sorting Method for Lithium-Ion Battery Reuse PLoS One, 2017. **12**(10): p. e0185922.

50.   Schneider, E., C. Oliveira, R. Brito, and C. Malfatti, Classification of Discarded Nimh and Li-Ion Batteries and Reuse of the Cells Still in Operational Conditions in Prototypes Journal of Power Sources, 2014. **262**: p. 1-9.

51.   Lyu, C., Y. Song, L. Wang, J. Li, B. Zhang, and E. Liu, A New Method for Lithium-Ion Battery Uniformity Sorting Based on Internal Criteria Journal of Energy Storage, 2019. **25**: p. 100885.

52.   An, F., J. Huang, C. Wang, Z. Li, J. Zhang, S. Wang, and P. Li, Cell Sorting for Parallel Lithium-Ion Battery Systems: Evaluation Based on an Electric Circuit Model Journal of Energy Storage, 2016. **6**: p. 195-203.

53.   Li, W., S. Chen, X. Peng, M. Xiao, L. Gao, A. Garg, and N. Bao, A Comprehensive Approach for the Clustering of Similar-Performance Cells for the Design of a Lithium-Ion Battery Module for Electric Vehicles Engineering, 2019. **5**(4): p. 795-802.

54.   Lai, X., C. Deng, J. Li, Z. Zhu, X. Han, and Y. Zheng, Rapid Sorting and Regrouping of Retired Lithium-Ion Battery Modules for Echelon Utilization Based on Partial Charging Curves IEEE Transactions on Vehicular Technology, 2021. **70**(2): p. 1246-54.

55.   Kampker, A., S. Wessel, F. Fiedler, and F. Maltoni, Battery Pack Remanufacturing Process up to Cell Level with Sorting and Repurposing of Battery Cells Journal of Remanufacturing, 2021. **11**(1): p. 1-23.

56.   Arora, S., A.T. Abkenar, S.G. Jayasinghe, and K. Tammi, *Chapter 6 - Charging Technologies and Standards Applicable to Heavy-Duty Electric Vehicles*, in *Heavy-Duty Electric Vehicles*, S. Arora, A.T. Abkenar, S.G. Jayasinghe, and K. Tammi, Editors. 2021, Butterworth-Heinemann. p. 135-55.

57.   Shafiei Sabet, P., G. Stahl, and D.U. Sauer, Non-Invasive Investigation of Predominant Processes in the Impedance Spectra of High Energy Lithium-Ion Batteries with Nickel–Cobalt–Aluminum Cathodes Journal of Power Sources, 2020. **472**: p. 228189.

58.   Dubarry, M., B.Y. Liaw, M.-S. Chen, S.-S. Chyan, K.-C. Han, W.-T. Sie, and S.-H. Wu, Identifying Battery Aging Mechanisms in Large Format Li Ion Cells Journal of Power Sources, 2011. **196**(7): p. 3420-5.

59.   Zheng, H., L. Zhang, G. Liu, X. Song, and V.S. Battaglia, Correlationship between Electrode Mechanics and Long-Term Cycling Performance for Graphite Anode in Lithium Ion Cells Journal of Power Sources, 2012. **217**: p. 530-7.

60.   Arora, S., A.T. Abkenar, S.G. Jayasinghe, and K. Tammi, *Chapter 5 - Ev Battery Pack Engineering—Electrical Design and Mechanical Design*, in *Heavy-Duty Electric Vehicles*, S. Arora, A.T. Abkenar, S.G. Jayasinghe, and K. Tammi, Editors. 2021, Butterworth-Heinemann. p. 105-34.

61.   Arora, S. and A. Kapoor, *Mechanical Design and Packaging of Battery Packs for Electric Vehicles*, in *Behaviour of Lithium-Ion Batteries in Electric Vehicles: Battery Health, Performance, Safety, and Cost*, G. Pistoia and B. Liaw, Editors. 2018, Springer International Publishing: Cham. p. 175-200.

62.   Kim, Y., Investigation of the Gas Evolution in Lithium Ion Batteries: Effect of Free Lithium Compounds in Cathode Materials Journal of Solid State Electrochemistry, 2013. **17**(7): p. 1961-5.

63.   Kim, Y., Mechanism of Gas Evolution from the Cathode of Lithium-Ion Batteries at the Initial Stage of High-Temperature Storage Journal of Materials Science, 2013. **48**(24): p. 8547-51.

64.   Somerville, L., J. Bareño, S. Trask, P. Jennings, A. McGordon, C. Lyness, and I. Bloom, The Effect of Charging Rate on the Graphite Electrode of Commercial Lithium-Ion Cells: A Post-Mortem Study Journal of Power Sources, 2016. **335**: p. 189-96.

65.   Harris, S.J., A. Timmons, D.R. Baker, and C. Monroe, Direct in Situ Measurements of Li Transport in Li-Ion Battery Negative Electrodes Chemical Physics Letters, 2010. **485**(4): p. 265-74.

66.   Qi, Y. and S.J. Harris, In Situ Observation of Strains During Lithiation of a Graphite Electrode Journal of The Electrochemical Society, 2010. **157**(6): p. A741.

67.   Rauhala, T., K. Jalkanen, T. Romann, E. Lust, N. Omar, and T. Kallio, Low-Temperature Aging Mechanisms of Commercial Graphite/Lifepo4 Cells Cycled with a Simulated Electric Vehicle Load Profile—a Post-Mortem Study Journal of Energy Storage, 2018. **20**: p. 344-56.

68.   Xu, J., Y. Jia, B. Liu, H. Zhao, H. Yu, J. Li, and S. Yin, Coupling Effect of State-of-Health and State-of-Charge on the Mechanical Integrity of Lithium-Ion Batteries Experimental Mechanics, 2018. **58**(4): p. 633-43.

69.   Rodriguez-Carvajal, J. *Fullprof: A Program for Rietveld Refinement and Pattern Matching Analysis*. in *satellite meeting on powder diffraction of the XV congress of the IUCr*. 1990. Toulouse, France:[sn].

70.   Ben Yahia, H., M. Shikano, and H. Kobayashi, Phase Transition Mechanisms in Li X Coo2 (0.25≤ X≤ 1) Based on Group–Subgroup Transformations Chemistry of Materials, 2013. **25**(18): p. 3687-701.

71.   Amatucci, G., J. Tarascon, and L. Klein, Coo2, the End Member of the Li X Coo2 Solid Solution Journal of The Electrochemical Society, 1996. **143**(3): p. 1114.

72.   Lahtinen, K., E.L. Rautama, H. Jiang, S. Räsänen, and T. Kallio, Reuse of Licoo2 Electrodes Collected from Spent Li-Ion Batteries after Electrochemical Re-Lithiation of the Electrode ChemSusChem, 2021. **14**(11): p. 2434-44.

73.   Wood III, D.L., J. Li, and C. Daniel, Prospects for Reducing the Processing Cost of Lithium Ion Batteries Journal of Power Sources, 2015. **275**: p. 234-42.

74.   Reeves, S. and R.S. Morris, Improved Mcmb Anodes by Surface Modification with Self-Assembling Nonionic Surfactants Electrochemical and Solid State Letters, 2004. **7**(8): p. B29.